Plume-ridge interactions: Ridge-ward versus plate-drag plume flow

Fengping Pang[1], Jie Liao[1,2,3], Maxim D. Ballmer[4], Lun Li[1,2,3]

[1]School of Earth Sciences and Engineering, Sun Yat-Sen University, Guangzhou 510275, China

[2]Guangdong Provincial Key Lab of Geodynamics and Geohazards, Guangzhou 510275, China

[3]Southern Marine Science and Engineering Guangdong Laboratory (Zhuhai), Zhuhai 519000, China

[4]Department of Earth Sciences, University College London, London, United Kingdom

Correspondence: Jie Liao (liaojie5@mail.sysu.edu.cn)

Abstract

The analysis of mid-ocean ridges and hotspots that are sourced by deep-rooted mantle plumes allows us to get a glimpse of mantle structure and dynamics. Dynamical interaction between ridge and plume processes have been widely proposed and studied, particularly in terms of ridge-ward plume flow. However, the effects of plate drag on plume-lithosphere and plume-ridge interaction remain poorly understood. In particular, the mechanisms that control plume flow towards vs. away from the ridge have not yet been systematically studied. Here, we use 2D thermomechanical numerical models of plume-ridge interaction to systematically explore the effects of (i) ridge spreading rate, (ii) initial plume head radius, and (iii) plume-ridge distance. Our numerical experiments suggest two different geodynamic regimes: (1) plume flow towards the ridge is favored by strong buoyant mantle plumes, slow spreading rates and small plume-ridge distances; (2) plume drag away from the ridge is in turn

21 promoted by fast ridge spreading, for small-to-intermediate plumes and large plume-ridge distance.

22 We find that the pressure gradient between the buoyant plume and spreading ridge at first drives

23 ridge-ward flow, but eventually the competition between plate drag and the gravitational force of

24 plume flow along the base of the sloping lithosphere controls the fate of plume (spreading towards vs.

25 away from the ridge). Our results highlight that fast-spreading ridges exert strong plate dragging

26 force, which sheds new light on natural observations of largely absent plume-lithosphere interaction

27 along fast-spreading ridges, such as the East Pacific Rise.

1 Introduction

Mid-ocean ridges (MORs) and hotspots are two main regions for deep material recycling to the surface of the Earth. However, these two units are not always isolated, but rather show strong interactions in some cases, termed as plume-ridge interaction (Morgan, 1978). Of up to 50 mantle plumes revealed by seismic tomography (French and Romanowicz, 2015; Montelli et al., 2004), more than 20 plumes are found to be associated with nearby ridges (Fig.1a; Ito et al., 2003). Plume-ridge interaction is manifested by geophysical and geochemical anomalies along the ridge axis, e.g., high mantle potential temperature (Dalton et al., 2014), enriched radiogenic isotope anomalies (Cushman et al., 2004; Douglass and Schilling, 1999; Yang et al. 2017), and adjacent lineations of seamounts (Ballmer et al., 2013b; Geissler et al., 2020; Lénat and Merle, 2009). Furthermore, plumes may promote migration of MOR spreading centers (Müller et al., 1998; Mittelstaedt et al., 2008, 2011; Whittaker et al., 2015), as evidenced by successive ridge jumps towards mantle plumes, e.g., at Iceland, Amsterdam-Saint Paul and Galapagos hotspots (Hardarson et al., 1997; Maia et al., 2011; Mittelstaedt et al., 2012). The interaction dynamics of a ridge with a ridge-centered and off-ridge plume has been widely studied and modeled in analogue and numerical experiments, revealing that the major controlling factors involve the ridge spreading rate, plume buoyancy flux and their spatial distance (François et al., 2018; Ito et al., 1997; Kincaid et al., 1996; Ribe et al., 1995; Ribe, 1996; Sleep, 1997). Indeed, most plume-ridge interaction systems are associated with slow-spreading ridges and small mantle plumes and short plume-ridge distances (Fig.1b). However, numerical studies systematically investigating the effects of these parameters on plume-ridge interaction and quantify the controlling forces remain scarce.

51   As has been noted previously, buoyant plumes tend to spread ridge-ward along the sloping base

52   of the lithosphere (Morgan, 1978; Schilling, 1991; Small, 1995). Regions of divergent mantle flow

53   beneath MORs represent the lowest dynamic-pressure regions in the oceanic asthenosphere, and thus

54   tend to suck ambient asthenospheric and plume materials towards the spreading center (Niu, 2014).

55   On the other hand, the viscous drag at the base of the plate tends to convey the spreading plume

56   material away from the MOR (Ribe and Christensen, 1994, 1999). Indeed, plume spreading at the

57   base of the lithosphere is governed by the competition of trench-ward viscous plate drag vs.

58   ridge-ward gravitational and pressure-driven forces (Kincaid et al.,1996). These gravitational and

59   tectonic forces compete with other to control the regime of plume-ridge interaction, but their balance

60   remains to be quantified.

61   The different distribution of hotspots with classified as plume-ridge interaction (ridge-ward

62   spreading) vs. no interaction (plate-drag spreading) also still remains enigmatic. Plume-ridge

63   interaction is much more common near the Mid-Atlantic ridge (MAR) than near the East Pacific Rise

64   (EPR) (Fig. 1a). Near the EPR, only the Pukapuka and Sojourn ridges display clear evidence of

65   ridge-ward flow of the magmatic source, but these volcanic ridges have been attributed to a

66   horizontally viscous differences or small-scale convection in uppermost mantle, and not a mantle

67   plume (Ballmer et al., 2013b; Clouard and Bonneville, 2005; Harmon et al., 2011). A previous study

68   (Jellinek et al., 2003) proposed that fast-spreading ridges guide upwelling mantle flow towards the

69   spreading center to convey the surrounding plumes from deep depth entirely into the MOR melting

70   zone (Fig. 1c), resulting in the absence of hotspots adjacent to the EPR (see also Rowley et al., 2016;

71   Rowley and Forte, 2022). However, fast plate spreading also tends to drag mantle plumes away from

72   the MOR (Kincaid et al., 1995, 1996), leading to the typically parabolic shapes of hotspot swells

73 such as near Hawaii (Ribe and Christensen, 1994). Whether the increased spreading rates in the

74 Pacific vs. Atlantic promote ridge-ward vs. plate-drag plume flow remains an intriguing question.

75   The principal goal of this study is to investigate the process of plume-ridge interaction, with an

76 emphasis on the effects of model parameters on the ridge-ward vs. plate-drag plume spreading. We

77 explore the effects of various model parameters, such as the size of the plume, ridge spreading rate,

78 and plume-ridge distance. Finally, we use our model results to interpret the difference of natural

79 plume-ridge interaction systems in different oceans, particularly the striking difference between the

80 East Pacific and Atlantic in this regard.

81
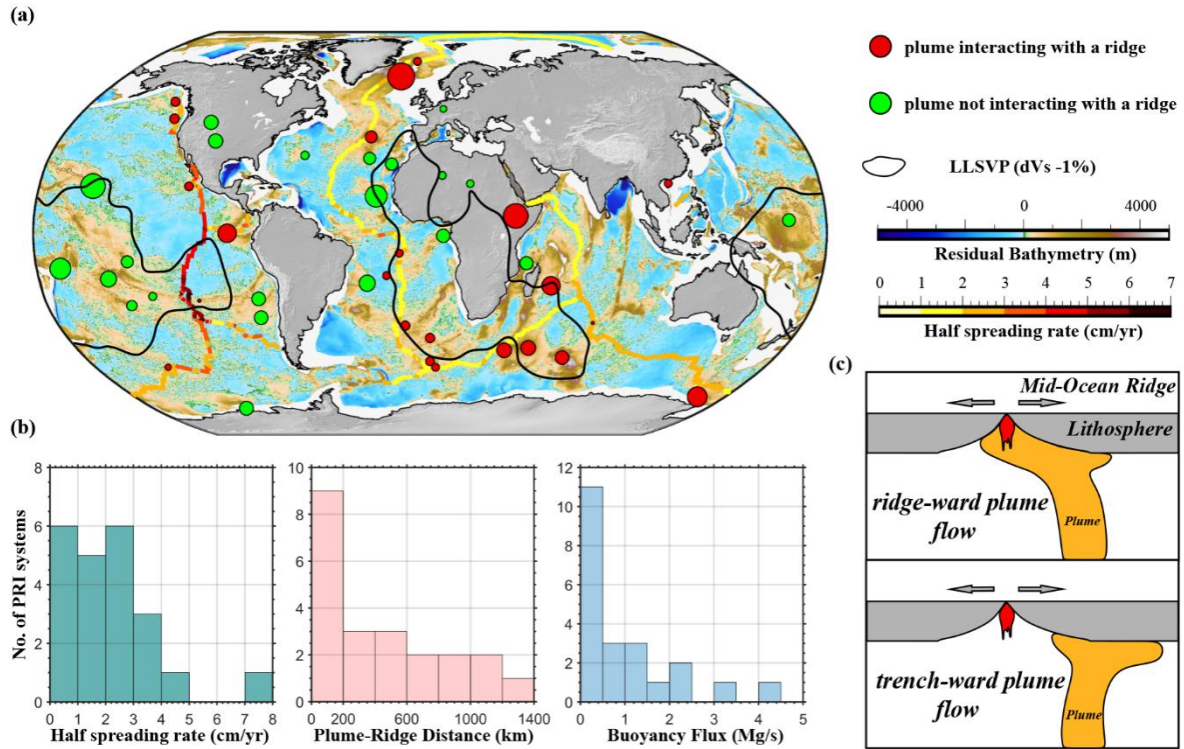
Figure 1. Global plume-ridge interaction systems. **(a)** Global distribution of mid-ocean ridges and mantle plumes. Residual bathymetry of the ocean basins come from Straume et al. (2019). Mid-ocean ridges are painted in color solid lines corresponding to half-spreading rate. Plumes not interacting with a ridge are shown by green circles, and hotspots linked to ridges are in red dots (Ito et al., 2003); size refers to the plume buoyancy flux from Hoggard (2020). Black lines denote the regions of two LLSVPs under the South Africa and Pacific Ocean (Torsvik et al., 2006). **(b)** Histograms of influential factors of plume-ridge interaction systems. Half spreading rate and plume-ridge distance is taken from GPlates (Müller et al., 2016; Whittaker et al., 2015). Plume-ridge interaction systems link to slow-spreading ridge and small mantle plumes and short plume-ridge distance. **(c)** Sketches of ridge-ward (top panel) and plate-drag plume flow (bottom panel) mode proposed, respectively.

Figure 2. Model setup. **(a)** Initial composition and boundary conditions. The oceanic plate consists of half-space cooling part and the thermal equilibrium part. A 50-Myrs-old mid-ocean ridge sets in the middle of the model based on half-space cooling temperature structure. A thermal and chemical anormal mantle plume locates at 660 km. Different colors indicate the initial rock types and corresponding newly formed molten rock types. Yellow arrows are the half-spreading rates imposed internal in the lithosphere (i.e., from 20 km to 120 km in depth) to simulate ridge spreading. **(b)** Initial tested ridge and plume configurations. **(c)** Initial tested plume-ridge distances.

2 Numerical modelling

2.1 Modelling methods

To explore plume-lithosphere and plume-ridge interaction, we conduct numerical simulations

106 utilizing the 2D thermo-mechanical code I2VIS, which is based on staggered finite difference

107 method combined with marker-in-cell techniques (Gerya and Yuen, 2003, 2007). The equations of

108 conservation of mass, momentum and energy (Eq. (1)-(3), respectively) are solved in a fully

109 staggered grid assuming an incompressible media:

110 $$\nabla \cdot \vec{v} = 0 \quad (1)$$

111 $$\frac{\partial \sigma'_{ij}}{\partial x_j} - \frac{\partial P}{\partial x_i} + \rho g_i = 0 \quad (2)$$

112 $$\rho C_p \left(\frac{DT}{Dt} \right) = - \nabla \cdot \vec{q} + H_r + H_a + H_s + H_l \quad (3)$$

113 where v refers to the velocity, σ'_{ij} the deviatoric stress tensor, P the pressure, ρ the density, g the

114 gravity acceleration, $\frac{D}{Dt}$ the Lagrangian time derivative, C_p the heat capacity, and q the heat flux.

115 Additionally, H_r, H_a, H_s, and H_l are the radioactive, adiabatic, shear, and latent heat productions,

116 respectively.

117   We employ a non-Newtonian visco-plastic rheology (Gerya and Yuen, 2007) in the models. The

118 viscous rheology depends on stress, temperature and pressure. The appropriate viscosity is expressed

119 as that of a composite diffusion and dislocation-creep material (Eq. (4)).

120 $$\frac{1}{\eta_{vis}} = \frac{1}{\eta_{diff}} + \frac{1}{\eta_{disl}} (4)$$

121 in which η_{diff} and η_{disl} are the diffusion and dislocation creep viscosity, respectively, and can be

122 further computed as Eq. (5) and Eq. (6):

123 $$\eta_{diff} = \frac{1}{2} A \sigma_{crit}^{1-n} \exp\left(\frac{PV_a + E_a}{RT} \right) \quad (5)$$

124 $$\eta_{disl} = \frac{1}{2} A^{\frac{1}{n}} \dot{\varepsilon}_{II}^{\frac{1-n}{n}} \exp\left(\frac{PV_a + E_a}{nRT} \right) \quad (6)$$

125 where P is the pressure, T is the temperature, $\dot{\varepsilon}_{II}$ is the second invariant of the strain rate tensor,

126 σ_{crit} is the diffusion-dislocation creep transition stress, and A, E_a, V_a, and n are the strain rate

127 pre-exponential factor, activation energy, activation volume, and stress exponent, respectively. The

128 plastic behavior η_{pla} is described by the Drucker-Prager yield criterion (Byerlee, 1978; Ranalli,

129 1995) according to Eq. (7) and Eq. (8):

$$\sigma_y = C + P\varphi \quad (7)$$

$$\eta_{pla} = \frac{\sigma_y}{2\dot{\varepsilon}_{II}} \quad (8)$$

132 in which σ_y is the yield stress, C is the rock cohesion and φ is the effective friction coefficient.

133 The effective viscosity η_{eff} of rocks is thus constrained by both viscous and plastic deformation,

134 where the rheological behavior depends on the minimum viscosity attained between ductile and

135 brittle fields:

$$\eta_{eff} = \min\left(\eta_{vis}, \eta_{pla}\right) \quad (9)$$

137   Partial melting, melt extraction and percolation are also considered in the model in a simplified

138 way (Gerya, 2013). The melt fraction (M_0) of the crust are assumed to increase with temperature and

139 are calculated according to Eq. (10):

$$M_0 = 0 \text{ when } T \leq T_{solidus}$$

$$M_0 = \frac{(T - T_{solidus})}{(T_{liquidus} - T_{solidus})} \quad \text{when } T_{solidus} < T < T_{liquidus} \quad (10)$$

$$M_0 = 1 \text{ when } T \geq T_{liquidus}$$

143 where $T_{solidus}$ and $T_{liquidus}$ are the solidus and liquidus temperature of different rock types,

144 respectively, taken from Katz et al. (2003).

145   In our model, melt extraction is modeled indirectly and considered as an instantaneous process

146 (Gerya et al., 2015). The extracted melt is assumed to move vertically from the molten source and

147 then added to the bottom of the crust. Partial melt is extracted from the mantle and instantaneously

148 displaced to the bottom of the crust and converted into hot mafic magma, obeying the conservation

149 of material. The amount of extracted melt during the evolution of each experiment is traced by the

150   Lagrangian markers (Gerya, 2013). The total amount of melt, M, for every marker excludes the

151   amount of previously extracted melt according to Eq. (11):

$$M = M_0 - \Sigma_n M_{ext} \quad (11)$$

153   where $\Sigma_n M_{ext}$ refers to the total melt fraction extracted during the previous n melt extraction

154   timesteps.

155   The effective density of mafic magma and molten crust depends on its melt fraction and is

156   calculated as (Gerya et al., 2015; Gülcher et al., 2020):

$$\rho_{eff} = \rho_{solid}(1 - M + M\frac{\rho_{0,molten}}{\rho_{0,solid}}) \quad (12)$$

158   where $\rho_{0,molten}$ and $\rho_{0,solid}$ are the reference densities of the molten and solid crust. ρ_{solid} is the

159   crust density at given pressure and temperature, which can be computed as:

$$\rho_{solid} = \rho_{0,solid}[1 - \alpha(T - 298)][1 + \beta(P - 0.1)] \quad (13)$$

161   with thermal expansion $\alpha = 3 \times 10^{-5} K^{-1}$ and compressibility $\beta = 10^{-11} Pa^{-1}$.

162   Surface processes, such as erosion and sedimentation, are considered by solving the transport

163   equation on the Eulerian nodes at each time step (Gerya and Yuen, 2003). Our erosion/sedimentation

164   model uses gross-scale erosion/sedimentation rates which are independent of local elevation and

165   topography (Burov and Cloetingh, 1997). We use constant and moderate rates of erosion (0.315

166   mm/yr) and sedimentation (0.0315 mm/yr), respectively, which falls within naturally observed

167   ranges.

168

169   **2.2 Model setup**

170   The size of the model box is 6600 × 1200 km, with a nonuniform grid of 501 × 301

171   computational nodes in length and depth, respectively (Fig. 2). The densest grid is located in the

172 center of the model domain (i.e., grid size decreases linearly from 20 km at the edges to 2 km at the

173 ridge axis, and increases linearly from 1 km at the top to 7 km at the bottom), where plume-ridge

174 interaction would happen. The model consists of a 20 km thick sticky air layer to accommodate

175 crustal surface deformation. To reproduce the oceanic lithosphere, we choose a typical layered model,

176 where the crust is composed of a water level (2 km), a sediment layer (1.5 km), and a basalt layer

177 (7.5 km). The oceanic lithosphere and asthenosphere in the model are both modeled as dry olivine

178 (the different colors for the mantle lithosphere and asthenosphere in the figures of this paper are only

179 for better visualization). Besides, a 50-Myrs-old mid-ocean ridge is set on central part of the

180 lithosphere, splitting the model domain into two parts. At the depth of 660 km, a 200-km-wide

181 semicircular plume is located on the left of model domain, corresponding to the onset of plume-ridge

182 interaction from the mantle transition zone. Detailed rock parameters are listed in Table 1.

183 The thermal conditions at the top and bottom boundaries are fixed at 273 and 2513 K,

184 respectively. The left and right boundaries are both insulating, with no external heat flow across them.

185 The initial temperature structure of the mantle is adiabatic (0.5 K km^{-1}), which results in a

186 temperature at 660 km depth of 1843 K. The initial temperature structure of the oceanic plate

187 consists of half-space cooling part and thermal equilibrium part (Fig. 2a). The half-space cooling

188 model is used to describe the oceanic plate younger than 50 Myr, and the thermal equilibrium

189 structure is used to describe older oceanic parts. In other words, the thermal age of the lithosphere far

190 away from the ridge is fixed at 50 Myr with a constant plate thickness (i.e., ~100 km). The hot plume

191 is set a circular thermal and compositional (see Table 1) anomaly with an excess temperature of 250

192 K to trigger a rising thermochemical plume. All the velocity boundaries are free slip boundaries.

193 Additional internal boundary velocities are imposed at 500 km from each side boundary in the

194   lithosphere to maintain the imposed half spreading rate (Fig. 2a).

195

196   **Table 1**. Rock physical properties used in the numerical models.

Parameters	Sediments	Ocean Crust	Mantle	Plume	Reference [a]
Flow law	Wet quartz	Basalt	Dry olivine	Wet olivine	
Preexponential factor $A(Pa^n s)$	1.97×10^{17}	4.80×10^{22}	3.98×10^{16}	5.01×10^{20}	1
Activation energy $E_a(KJ\ mol^{-1})$	154	238	532	470	1
Activation volume $V_a(J\ bar^{-1}mol^{-1})$	0	0	1	0.8	1
Exponent n	2.3	3.2	3.5	4	1
Cohesion $C(Pa)$	2×10^7	2×10^7	2×10^7	2×10^7	1
Effective friction coefficient φ	0.6/0.3	0.6/0.3	0.6/0.3	0.6/0.3	1
Density $\rho(Kg\ m^{-3})$	2600	3000	3300	3270	2
Radioactive heating $H_r(W\ m^{-3})$	2×10^{-6}	2.2×10^{-7}	2.2×10^{-8}	2.5×10^{-8}	2

197   a: 1-(Ranalli, 1995), 2-(Turcotte and Schubert, 2014)

198   Other physical parameters used for all rocks include: gas constant R=8.314 J K^{-1}mol^{-1}, thermal

199   expansion α=3×10^{-5} K^{-1}, compressibility β=1×10^{-11} Pa^{-1}, heat capacity Cp=1000 J kg^{-1}K^{-1}.

200

201   **3   Model Results**

202   We conduct a series of numerical experiments to investigate ridge suction versus plate drag acts

203   on plumes. The effects of three major model parameters (i.e., the spreading rate of mid-ocean ridge,

204   the initial plume head radius, and the plume-ridge distance) are systematiclly studied. The typical

205   dynamic evolution of models with ridge-ward vs. plate-drag plume flow are demonstrated.

206   **3.1 Model evolution with ridge-ward plume flow**

207   For models with dominant ridge-ward flow, the typical model evolution is shown in Fig. 3 (the

208   major model parameters used in this case are: the half spreading rate of 8 mm yr^{-1}, the initial plume

209 head radius of 200 km, and the off-axis distance of 800 km). In the early plume head stage, the

210 buoyant mantle plume rises up rapidly in a mushroom-like shape and imposes dynamic stresses at the

211 base of the overriding oceanic plate, leading to significant surface uplift (Figs. 3a,b). The ascending

212 plume experiences extensive decompression melting at the base of the overriding plate, and due to

213 the dynamic overpressure, spreads laterally, forming two branches that flow in opposite directions

214 (Fig. 3c). A large amount of plume material is eventually entrained towards the spreading center,

215 ponding underneath the ridge axis, and significantly affecting the ridge dynamics. The entrainment of

216 hot plume material promotes decompression melting (Figs. 3d, e) and increases the temperature

217 beneath the ridge (Fig. S2). Within the overlying lithosphere, the buoyant mantle plume leads to

218 stress localization and strongly weakens the oceanic plate (Figs. S1, S3). As the plume eventually

219 flows upward along the base of the gradually sloping plate near MOR, melting and crust production

220 occurs (Fig. S1), forming an oceanic plateau of thickened crust. In addition to this gravitational force

221 that guides plume material of the right branch ridge-ward, plate spreading drags both branches in the

222 opposite direction. Moreover, convective and tectonic stresses ("plume push" and "ridge suction")

223 affect both branches of the plume in a different way. As a consequence, the two branches evolve

224 asymmetrically: the right branch that flows towards the ridge axis is more vigorous than the left

225 branch, and the plume tail is also tilted towards the spreading center (Figs. 3c-e).
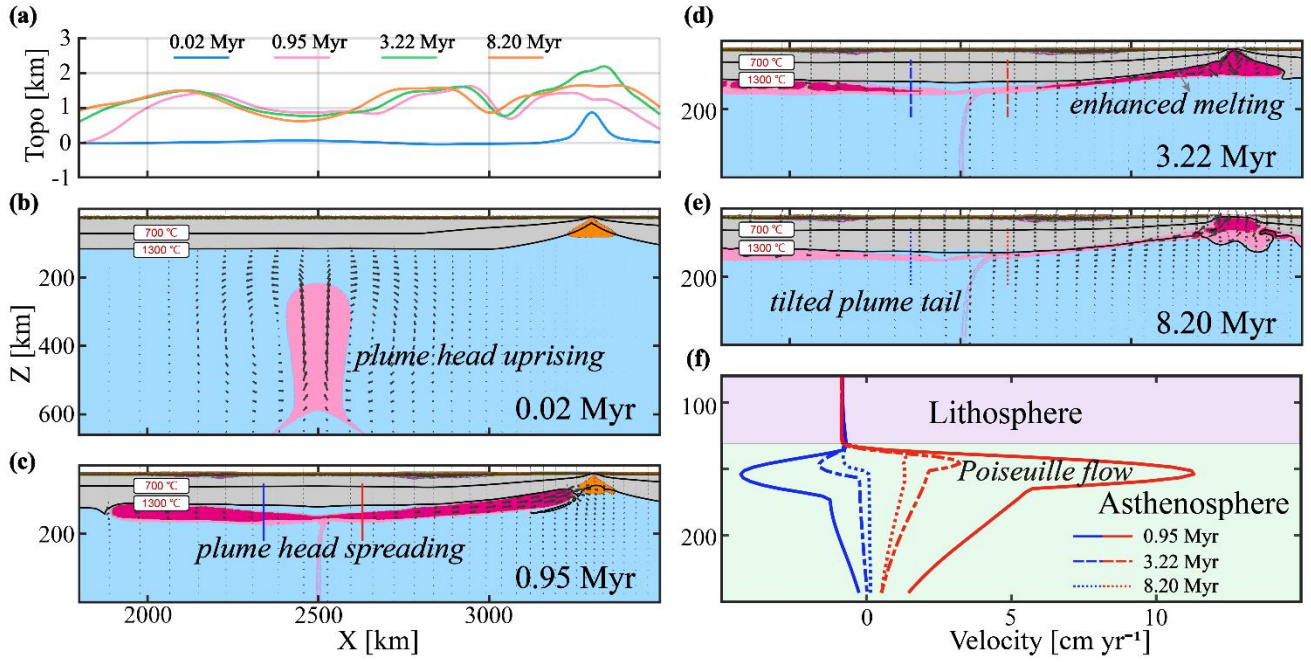
Figure 3. The evolution of the reference model M12 (see Table S1 in supplementary material) with dominant ridge-ward plume flow. The main model parameters employed in this case are: half spreading rate of 8 mm yr⁻¹, an initial plume head radius of 200 km, and an off-axis distance of 800 km. **(a)** surface topography over time along the flow path. **(b-e)** Snapshots of composition for the reference model (M12). **(f)** Profiles of the horizontal velocity component over time at the sections as indicated (color-coded) in panel (c-e).

The mantle flow horizontal velocity profiles (Fig. 3f) further demonstrate the dominance of ridge-ward plume flow, showing that plume flow is faster towards the spreading ridge than away from it. The velocity profiles elucidate dominant Poiseuille flow, with the maximum flow velocities in the middle of the asthenospheric channel. Such velocity profiles are well consistent with observations of seismic anisotropy at the Reunion plume (Barruol et al. 2019). The branches of the spreading plume head move significantly faster than the overriding plate. Because of the asymmetrical spreading of the plume head, the buoyancy flux carried by the right branch of the

241 plume (density anomaly multiplied by horizontal velocity from Figure 3f) is also much larger than

242 that carried by the left branch.

243

244 **3.2 Model evolution with plate-drag plume flow**

245 For models with dominant plume flow away from the ridge ("plate-drag flow"), the typical

246 model evolution is shown in Fig. 4. The controlling parameters of the representative model shown in

247 Figure 4 are the same as for the model shown in Figure 3, except for a smaller radius (100 km) and

248 faster spreading ridge (half spreading rate: 45 mm yr^{-1}). At first, the ascending plume head spreads

249 out similarly as in the case described above and interacts with the overriding oceanic lithosphere.

250 The largest surface uplift is sustained just above the plume head (Fig. 4a), slightly different from the

251 previous model in which the highest surface elevation is observed on both sides of the plume conduit

252 (Fig. 3a). Related to this spreading and uplift, the mantle plume changes the stress state of the

253 overlying oceanic plate (Fig. S4), resulting in a slightly weakening (Fig. S6). The plume head

254 undergoes significant decompression melting near the deflection point (Fig. 4c). However, it is

255 difficult for small plume to extract molten plume due to the low melt flux. (Fig. S4). As the plume

256 cools, partially molten plume gets solidified speedily (Figs. 4d-e and S5). In contrast to the reference

257 model from section 3.1, this model displays most plume material flowing away from the ridge, likely

258 due to dominant plate drag (Figs. 4c-e). Indeed, the left branch of the plume consistently displays

259 larger buoyancy fluxes and maximum velocities than the right side over time (Fig. 4f).

260
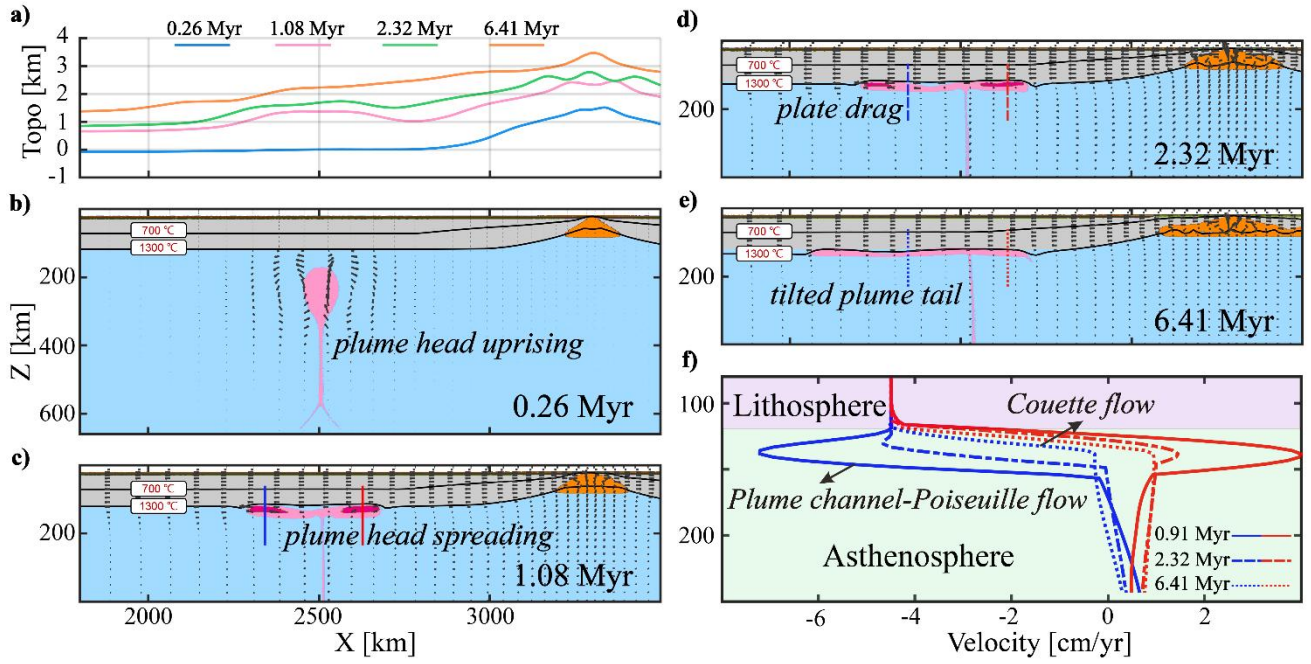
Figure 4. Same as Figure 3 for case M77 (i.e., the reference model for the plate-drag plume flow regime). The main model parameters employed in this case are: half spreading rate of 45 mm yr⁻¹, an initial plume head radius of 100 km, and an off-axis distance of 800 km.

The underlying mechanism for dominant plate-drag plume flow is the frictional shear force of the moving plate, which is further demonstrated by the plume flow velocity profiles (Fig. 4f). In the early plume head stage (~1.08 Myr), the plume spreads out faster than plate velocity, which is primarily driven by the overpressure of the ponding plume head at this stage. After a short amount of time (~2.32 Myr), however, plume spreading becomes significantly slower than plate velocity, and hence plate drag drives and controls the plume flow. Indeed, the flow mode in the asthenosphere rapidly shifts from Poiseuille flow (i.e., active plume flow) to Couette flow (i.e., passive plume flow) (Fig. 4f), indicating the increasing role of plate drag on plume flow, soon after an initial of plume-head spreading.
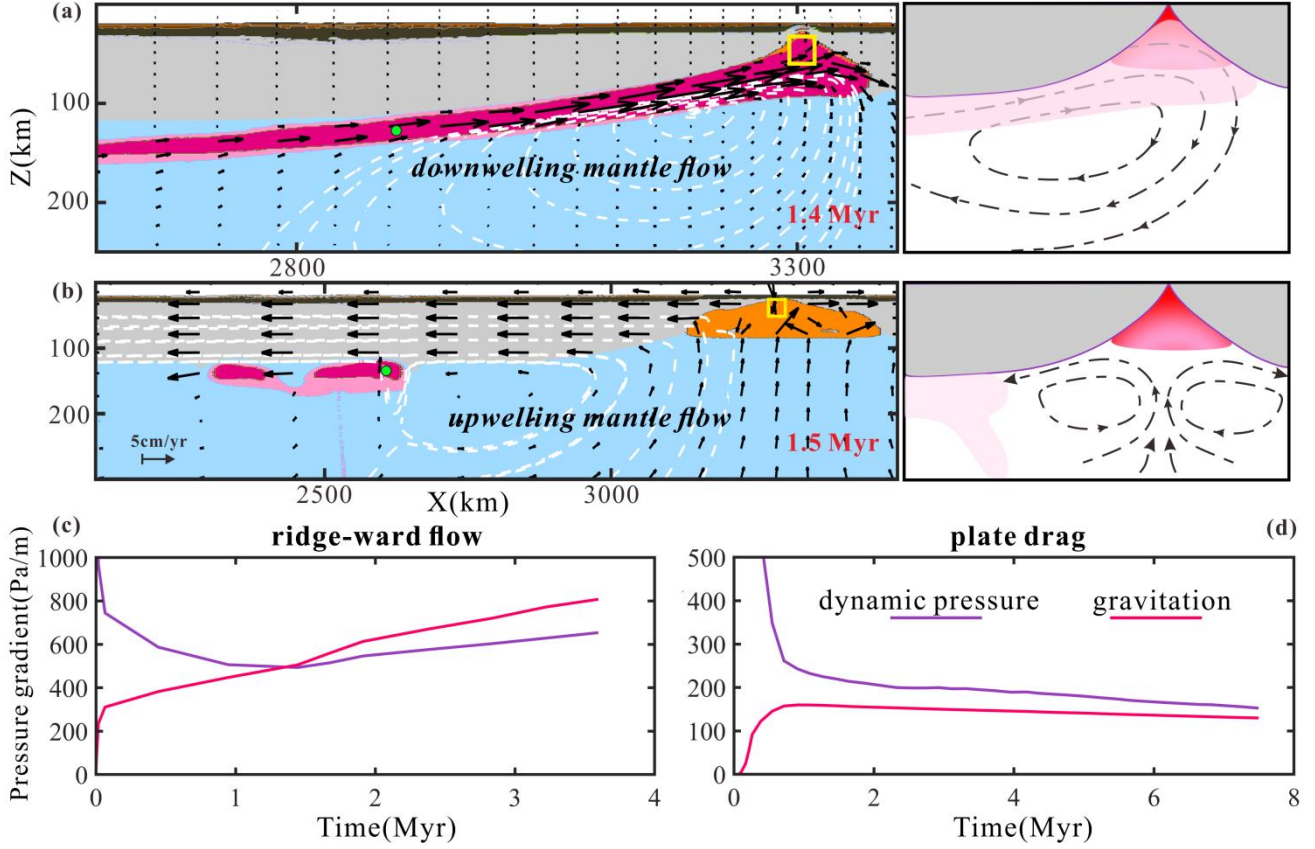
Figure 5. Comparsion between models with ridge-ward vs. plate-drag plume flow. **(a)** Ridge-ward

flow with downwelling beneath the MOR (results from case M12 as in Figure 3). White dashed lines

are streamlines; black arrows visualize the flow field. Schematic of flow in the sub-panel on the

right-hand side. **(b)** Plate-drag flow with upwelling mantle corner flow beneath the MOR (results

from case M77 as in Figure 4). **(c)** The dynamic pressure and gravitational gradient of plume marker

(i.e. green circle in (a)) over time. **(d)** The dynamic pressure and gravitational gradient of plume

marker (i.e. green circle in (b)) over time. The yellow box marks the location for the computation of

average dynamic pressure at the ridge, needed for the calculation of the dynamic pressure gradient

(see text). The (c) and (d) are representing the results of ridge-ward and plate drag flow, respectively.

3.3 Two modes of plume-lithosphere interaction

288   The dominant ridge-ward and dominant plate-drag plume flow regimes are two distinct modes of

289   plume-plate interaction. The differences between these two regimes are further demonstrated in

290   terms of mantle flow (Figs. 5a,b), driving forces (Figs. 5c,d).

291   In the ridge-ward dominated models, clockwise mantle develops from the plume to the spreading

292   ridge (Fig. 5a). Molten plume material flows to the spreading ridge and occupies the space

293   underneath the ridge axis, sustaining significant asymmetry of mid-ocean ridge melting (Conder et

294   al., 2002). As a consequence to the continuous supply of the plume material, downward mantle flow

295   forms beneath the ridge axis. This flow pattern dramatically differs from that shown in the plate-drag

296   dominated models, which show upward mantle flow underneath the ridge axis (Fig. 5b), as typical

297   for the flow beneath a MOR without the influence of a plume.

298   The distinct modes of plume-ridge interaction (ridge-ward vs. plate-drag flow) are controlled by

299   the competition of the tectonic (plate drag, ridge suction) and gravitational (plume buoyancy) driving

300   forces. On one hand, the moving plate drags sub-lithospheric plume material away from the ridge.

301   On the other hand, the mechanism of ridge-ward flow is twofold. First, the buoyant plume material

302   flows along the sloping base of the lithosphere towards the shallow ridge along the gravitational

303   gradient. Second, the plume is driven along the dynamic-pressure gradient from the pressure

304   maximum (e.g., where the plume sustains dynamic topograph) towards the pressure minumum

305   beneath the diverging ridge. These gravitational (G_{gv}) and pressure-driven (G_{dp}) gradients are

306   calculated by tracing plume markers (Figs. 5c,d) as follows:

$$G_{dp} = (P_{mk} - P_r)/L \qquad (12)$$

$$G_{gv} = (\rho_0 - \rho_{mk}) * g * k \qquad (13)$$

309 where P_{mk} is the dynamic pressure of plume marker and P_r is the averaged pressure in a 50 km box

310 at ridge center (Fig. 5b); L is the horizontal distance from plume marker to ridge axis; ρ_{mk} and ρ_0

311 are the plume marker density and initial density, respectively; g is the gravitational acceleration; k is

312 the local slope of the base of the lithosphere.

313   In the early stage of model evolution, the plume head's dynamic overpressure is dominant,

314 driving plume spreading in both directions (Figs.5c,d), in particular in the direction of the

315 low-pressure ridge. However, this pressure gradient systematically diminishes over time as the plume

316 (head) spreads. Once the spreading plume approaches the ridge, the lithospheric slope increases. At

317 some point, the gravitational gradient exceeds the dynamic pressure gradient, taking over as the

318 major driving force of guiding plume material towards the ridge. However, for low flux plume, the

319 dynamic pressure and gravitation are not enough to support the flow to the ridge. Consequently, one

320 of the essential conditions for plume-ridge interaction is that the plume must be able to reach the

321 critical zone near the ridge, where the slope is sufficiently steep to take over for the ever diminishing

322 pressure gradient. This implies that the plume buoyancy must (1) overcome the shearing force of

323 plate drag, and (2) the pressure-gradient must be sustained long enough to reach the critical zone, in

324 which the gravitational gradient can take over. The (1) shearing force scales with the rate of ridge

325 spreading, and the (2) plume with high buoyancy flux is more likely to reach the critical region at a

326 given plume-ridge distance.

327

328

329 **3.4 Influence of model parameters**

330   We have systematically investigated the effect of the three main model parameters (i.e., the

spreading rate of the mid-ocean ridge, initial plume head radius and plume-ridge distance) on

plume-ridge interaction. We explored half spreading rates of the ridge of 8, 15, 30, and 45 mm yr^{-1},

corresponding to ultra-slow, slow, medium, and fast-spreading mid-ocean ridges, respectively (Gerya,

2012). We varied initial plume head radii in the range of 100 km to 300 km. Further, we tested

plume-ridge distance in the range of 600 to 1400 km.

3.4.1 Plume head radius

The size of the buoyant plume exerts an important control on plume-ridge interaction. Small

plumes tend to be dragged away from the ridge, with typically larger lateral fluxes of the left branch

than the right branch of the spreading plume (Figs. 6a,b). The buoyancy flux, defined as the integral

over a horizontal plane of the product of the vertical velocity and the density deficit within the plume,

in each branch is calculated by multiplying the velocity of the markers in plume pipe (Figs. 6d-f) by

the density. The dynamic pressure decreases with decreasing plume size (Fig. S8a), and the pressures

gradient is thus not strong enough for small plumes to reach the ridge. Plate shearing dominates

plume flow soon after plume head spreading, and the moving plate then drags plume head material,

leaving a tilted plume tail (Fig. 6d). In contrast, with larger initial plume head radius or buoyancy

flux, the ponding plume spreads more vigorously (Fig. 6c) and sustains much higher overpressures at

the base of the plate (Fig. S8a). This vigorous spreading can overcome plate drag to drive Poiseuille

flow in both directions. Once the right plume branch approaches the spreading center, it is attracted

and further accelerated by ridge suction. The plume tail is also markedly tilted towards the ridge axis

due to asymmetric spreading (Fig. 6f). The larger the plume is, the more plume material gets

entrained by the spreading center.
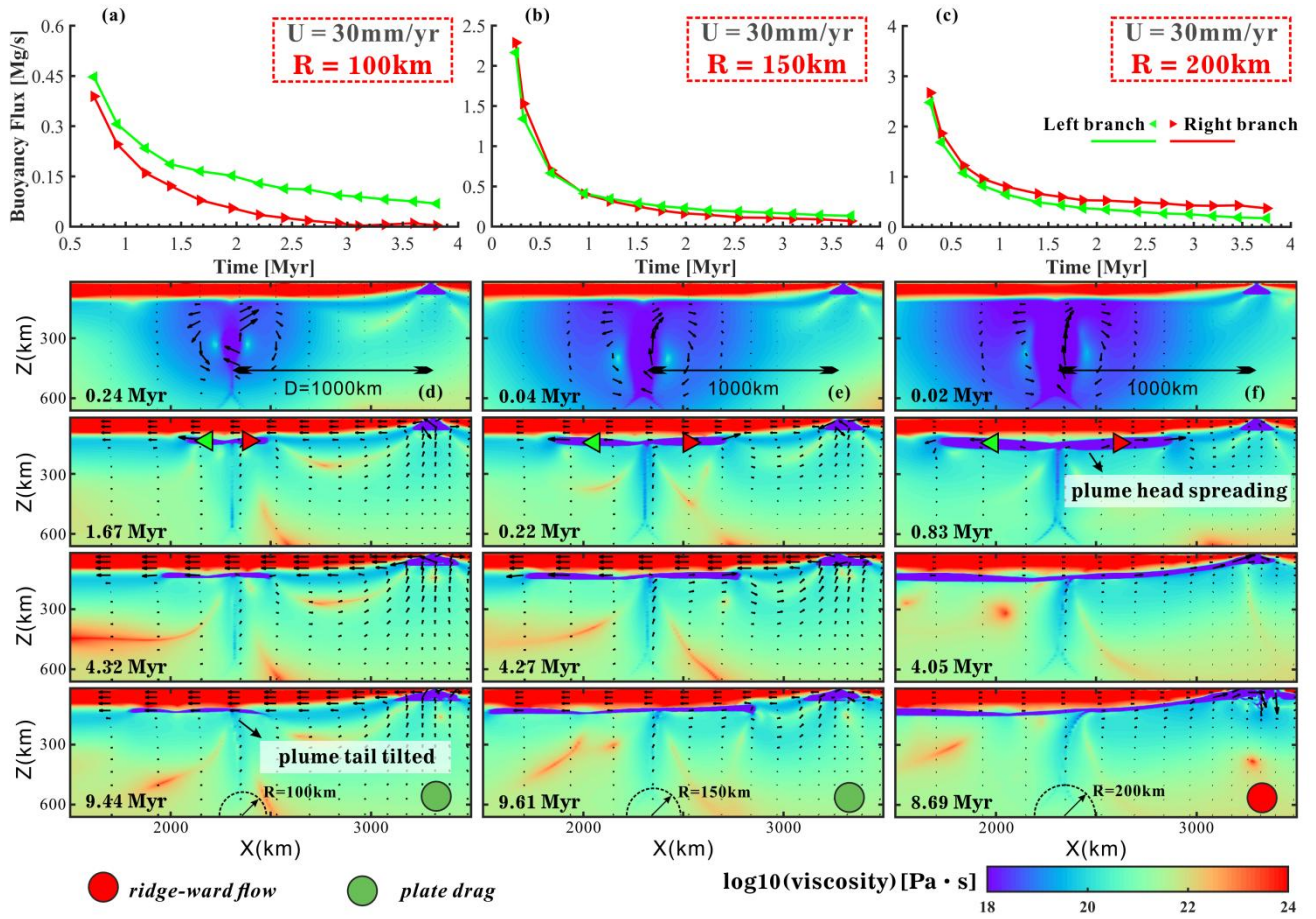
Figure 6 Models varying initial plume head radii (model M53, M58, and M63, Table S1 in supplementary material) shown by buoyancy flux and viscosity. **(a-c)** Buoyancy flux in spreading plume branches over time. Green and red triangles are markers used for buoyancy flux calculations of left and right plume branches, respectively. U and R stand for half of spreading rate and plume radius. **(d-f)** Viscosity snapshots of models with different plume head radii. Models with green circle represent plate-drag plume flow and ridge-ward plume flow in red.

3.4.2 Plume-ridge distance

Plume-ridge distance also controls the regime of plume-ridge interaction. A plume at large distances spreads similarly as a plume at a small distance, but is less likely to get affected by ridge suction (Fig. 7). The pressure gradient between the plume and ridge drives the ridge-ward plume

364 flow. However, the larger the plume-ridge distance, the smaller the pressure gradient would be (Fig.

365 S8b), resulting in a lower buoyancy flux across the plume pipe (Figs. 7a-c). In the cases of distant

366 plumes, the spreading of the plume head is strongly affected by plate drag (Figs. 7b, c).
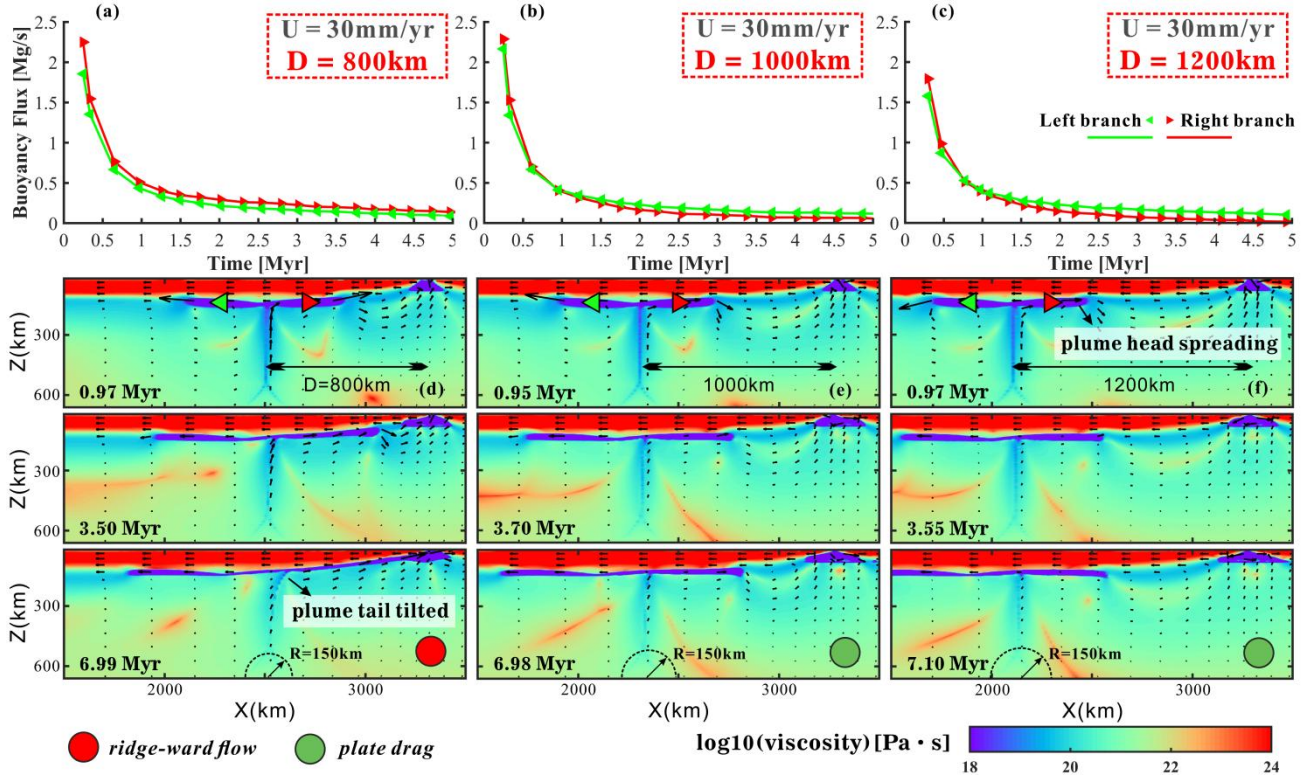
367

Figure 7. Models varying plume-ridge distances (model M57-M59, Table S1 in supplementary

369 material) shown by buoyancy flux and viscosity. **(a-c)** Buoyancy flux in spreading plume branches

370 over time. Green and red triangles are markers used for buoyancy flux calculations of left and right

371 plume branches, respectively. U and D stand for half of spreading rate and plume-ridge distance. **(d-f)**

372 Viscosity snapshots of models with different plume-ridge distances. Models with green circle

373 represent plate-drag plume flow and ridge-ward plume flow in red.

374

3.4.3 Half spreading rate of ridge

376   Another parameter that is worth investigating is the spreading rate of the ridge. The modeling

377 results indicate that fast-spreading ridges promote plume flow away from the ridge due to the friction

378   (Figs.8 and 9a). With increasing spreading rate, the effect of plate shearing on plume-lithosphere

379   interaction increases, as quantified by the spreading fraction. The spreading fraction γ (Eq.(14)) is

380   defined here as the ratio of ridge-ward vs. plate-drag plume volume fluxes. We integrated the

381   ridge-ward plume volume flux (right branch), V_{rw}, and plate-drag plume volume flux (left branch),

382   V_{tw}. V_p is the total plume volume flux in the model. Ridge-ward plume spreading is dominant for

383   positive γ; plate-drag plume spreading is dominant for negative γ.

384
$$\gamma = (V_{rw} - V_{tw})/V_p \qquad (14)$$

385   In the early stage (~1 Myr), pressure-driven flow dominates in all models and spreading

386   fractions are positive, mainly driven by the expansion of the overpressured plume heads along the

387   pressure gradient. After a certain time, the spreading fractions decrease dramatically with the decay

388   of the mantle plume activity, representing the transition from the ridge-ward to the plate-drag regime

389   in some cases. The characteristic spreading fractions after 8 Myr model time as a function of our

390   model parameters are shown in Fig. 8. This compilation of our results reveals that the dominance of

391   ridge-ward flow decreases with increasing spreading rate and off-axis distance, but significantly

392   increases with plume size. For models with fast-spreading ridges, the parameter range of plate-drag

393   flow dominated models is expanded, indicating the critical role of plate drag in restricting ridge-ward

394   flow and plume-ridge interaction.
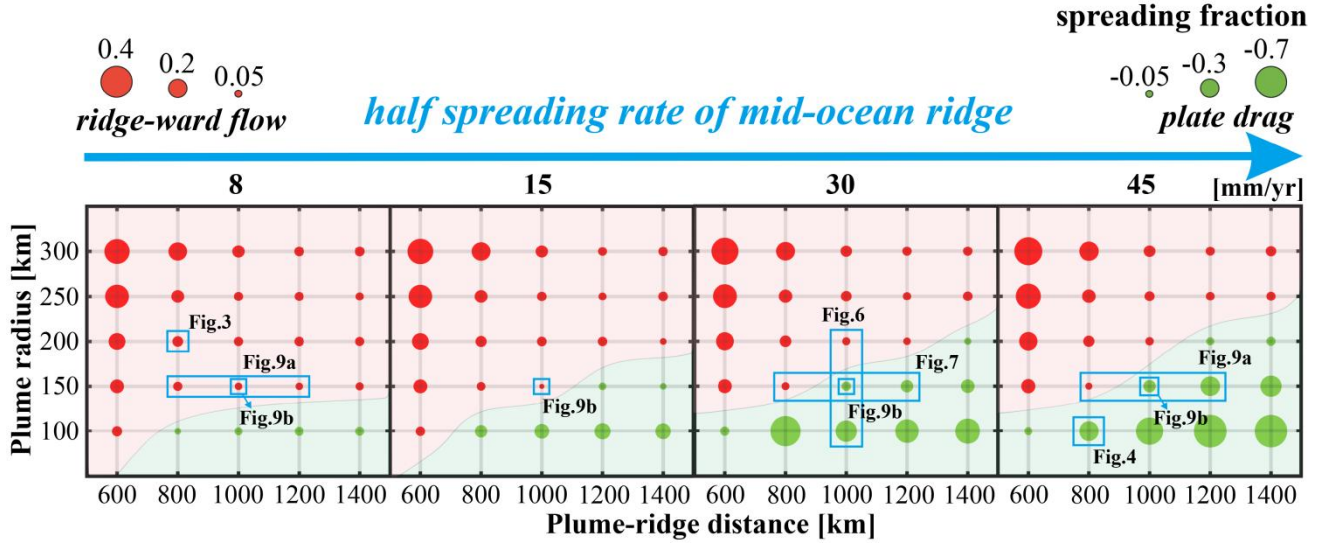
Figure 8. Parameter regime diagram of the contrasting modes of plume-ridge interaction. Spreading fractions γ (Eq. (14)) at ~8 Myr model time. Each of the circles represents one of the numerical experiments, and sizes refer to γ. Circles in red and green represent models with dominant ridge-ward plume flow and plate drag, respectively.

The transition from ridge-ward (positive γ) to plate-drag (negative γ) flow in some of our cases is mainly determined by the competition between the effects of pressure-driven plume head spreading and plate shearing. The overpressure in the plume head drives plume materials towards the lower pressure spreading center, while the moving plate shears plume away. Hence, we quantify the shear force of the overriding oceanic plate on the plume head using an integral approach:

$$F_s = \int \sigma_{xz}\, dA \quad (15)$$

Equation (15) is employed to calculate the shear force, where F_s is the total shear force the spreading oceanic plate exerts on the uppermost part of the plume. σ_{xz} is the shear stress on each mantle plume grid cell, A refers to the area of each grid cell. The pressure gradients, both

411   gravitational and dynamic pressure, are calculated by tracing the plume markers according to

412   equations (12-13). As the plume material rises to the base of the lithosphere, the shear force exerted

413   by the plate increases over time. We find that the integrated shear force between the spreading plate

414   and the plume increases significantly as half spreading rate increases (Fig. 9c).

415   Conversely, ridge spreading rates control gravitational and pressure-driven plume driving forces

416   (Fig. 9d). Increasing the spreading rate of the ridge implies a smaller dynamic pressure gradient,

417   because the pressure gradient is related to the plate thickness difference at the ridge and plume,

418   which is dependent on the spreading rate. A fast-spreading ridge also implies a smaller gravitational

419   gradient, because it leaves a more shallowly-dipping lithospheric base. Thus, relatively strong plate

420   shearing combined with relatively small pressure and gravitational gradients tend to advance

421   plate-drag plume flow for high spreading rates.
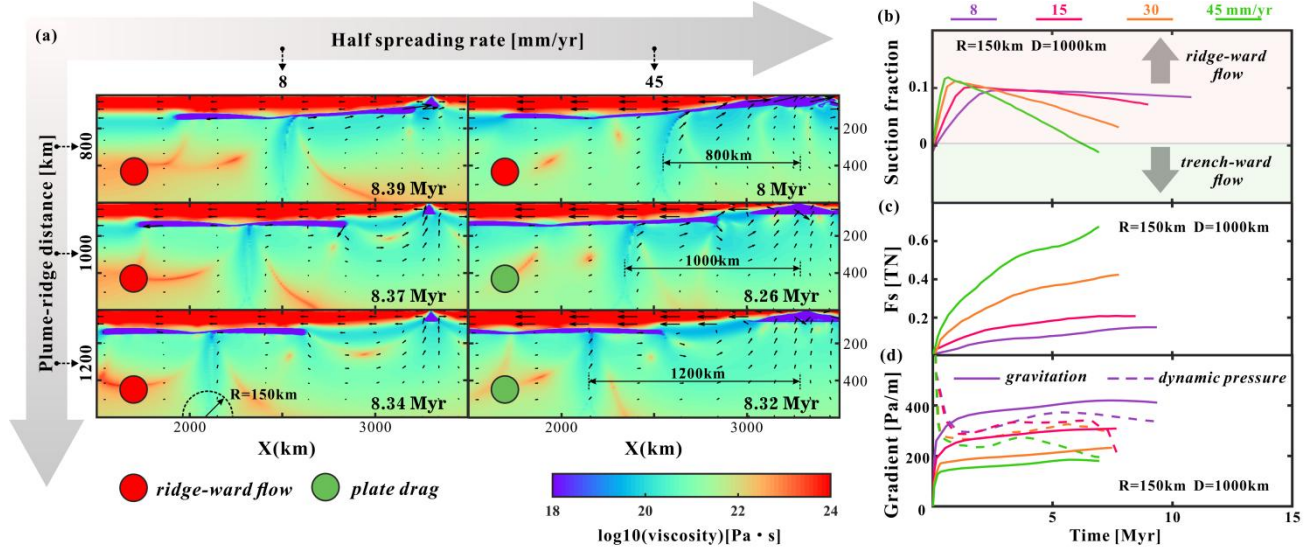
423   **Figure 9.** Model results influenced by different half spreading rates. **(a)** Effect of half spreading rate

424   and plume-ridge distance on ridge-ward vs plate-drag. Viscosity snapshots are shown (model M7-M9,

425   M82-M84, Table S1 in supplementary material). Fast-spreading ridge promotes plume material

426   dragged when plume near the ridge. Models with green circle represent plate-drag plume flow and

427 ridge-ward plume flow in red. **(b)** Dynamic evolutions of ridge-ward and plate-drag plume flow,

428 revealed by defined ridge spreading fraction (eq.14). **(c)** Shear force (*Fs*) between moving plate and

429 plume material under different spreading rates. **(d)** Pressure gradient between plume head and ridge

430 center in different half spreading rate models. The solid and dash lines are the plume gravitation and

431 dynamic pressure gradient, respectively. R and D stand for half of plume radius and plume-ridge

432 distance.

433

434

435 **4   Discussion**

436   Natural observations show that there are only very few hotspots indicative of ridge-ward plume

437 flow close to the East Pacific Rise (EPR) (Fig. 10a), in contrast to many such hotspots in the Atlantic

438 and Indian oceans. A previous study (Jellinek et al., 2003) proposed that fast-spreading ridges such

439 as the EPR efficiently convey any surrounding plumes into the spreading center from the deep

440 mantle (Fig. 1c), which leads to fewer hotspots nearby fast-spreading ridges. However, based on our

441 modeling results, fast-spreading ridges tend to promote plate-drag flow of the spreading plume

442 material, providing an alternative explanation to the relatively absence of hotspots along the EPR.

443 We discuss the possibility of this potential explanation combined with geological and geophysical

444 observations (Fig. 10).

445   Firstly, the plate drag effect of fast-spreading ridges on plumes is evidenced by geophysical

446 observations. We locate the positions of the mantle plumes at the core-mantle boundary (CMB) and

447 the associated hot spots on the surface based on global seismic tomography (Jackson et al., 2021;

448 Koppers et al., 2021). A lateral offset between the deep and surface positions of plumes is a common

feature, indicating the deflection of plumes due to mantle flow. Specifically, a large portion of (7 of 14) plumes located in the Atlantic are tilted towards the mid-ocean ridge. However, only very few plumes (6 of 16) in the Pacific are tilted towards the mid-ocean ridge. Indeed, the majority of plumes are tilted away from the ridges, indicating the significant effect of plate drag on plumes beneath fast plates. Such observations are consistent with the predictions of our models with dominant plate-drag plume spreading.
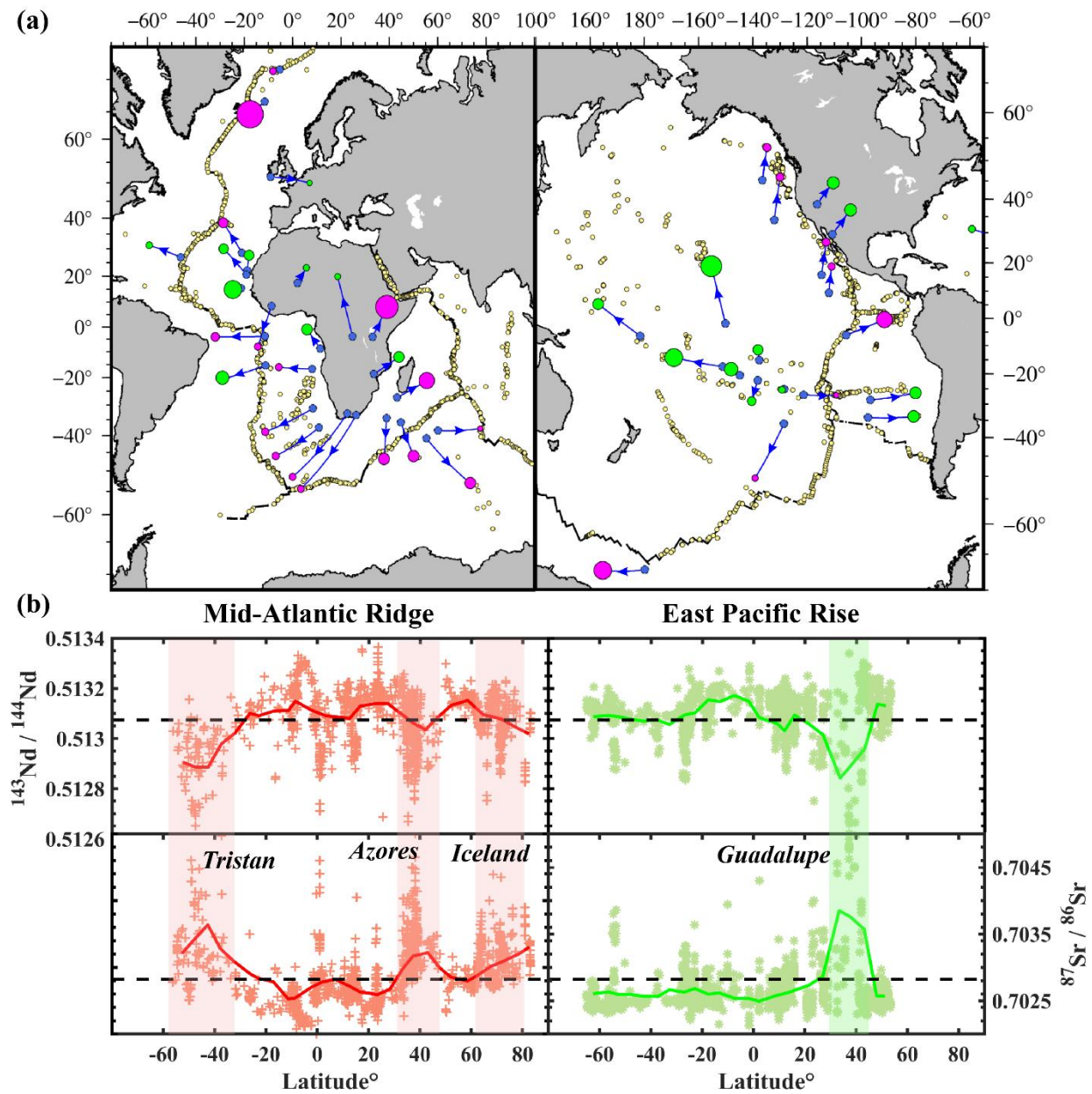
Figure 10. A compilation of hotspots along with spreading ridges in the Atlantic and the Pacific. **(a)**

457 Distribution of surface hotspots (circles) together with depth-projected source locations at CMB

458 (blue dots) of the plumes based on (Jackson et al., 2021). Plumes in magenta circles are mantle

459 plumes interacted with ridges (Ito et al., 2003), and plumes not interacted with ridges are shown as

460 green circles, whose size refers to the plume buoyancy flux (Hoggard et al., 2020). Blue arrows

461 indicate the changes in the position of the plume at the top and bottom of the mantle. Yellow dots are

462 MORB samples mapped in (b). **(b)** Plot of radioactive isotopes ratios along ridge MORB samples.

463 The data are downloaded from the PetDB Database (http://portal.earthchem.org/). The colored

464 symbols refer to samples in different mid-ocean ridge. Main hotspots influencing MORBs are

465 labeled with shaded bands. The black dash lines are the mean MORB isotopes ratio from Gale (2013).

466 Red and green lines are the mean ratios of the samples in Mid-Atlantic ridge and EPR, respectively.

467

468   Geochemical studies suggest that mantle plumes are enriched in light rare earth elements

469 (LREEs) and radiogenic isotopes of Sr and Pb but depleted in Nd isotopes. These geochemical

470 anomalies are evident in MORB at the sites of active plume-ridge interaction (Cushman et al., 2004;

471 Douglass and Schilling, 1999; Yang et al. 2017). We find that MORB sampled along both the

472 Mid-Atlantic ridge and the EPR indeed display geochemical anomalies (Fig. 10b), indicating

473 ridge-ward flow of plume material at specific locations. However, the Mid-Atlantic MORB dataset is

474 slightly more heterogeneous than the East Pacific Rise in terms of geochemical isotopes. The EPR is

475 basically characterized as normal oceanic basalt, along which only very few regions show

476 composition associated with nearby plumes. This contradicts the view (Jellinek et al., 2003) that

477 mantle plumes are fully entrained into the central MOR melting zone at fast-spreading ridges.

478   Based on our modeling results, initial plume head radius and plume-ridge distance also control

479   the mode of plume-ridge interaction. However, for different buoyancy fluxes B, there is only a small

480   difference in the proportion of interacting plumes to non-interacting plumes. A small majority of

481   major plumes (5 of 8 with $B > 1.6$ Mg/s), and a small minority of small-to-intermediate plumes (11

482   of 25 for $B < 1.6$ Mg/s) display interaction with the ridge (Fig. 11a). The underlying cause for this

483   observation remains unclear, but may be related to the distribution of large plumes globally with

484   many of them being located very far from MORs. Also note that our 2D models are limited in that

485   plume material cannot spread in the out-of-plane direction, hence somewhat exaggerating the effects

486   of buoyancy flux. In any case, the distribution of observed plume buoyancy fluxes (Hoggard et al.,

487   2020) varies little across different oceans (Fig. 11a). Therefore, the effects of plume size are not a

488   good candidate to explain the notable difference between the Atlantic and Pacific in terms of

489   plume-ridge interaction mode.

490   On the other hand, compared with the Atlantic and Indian Oceans, Pacific plumes are located

491   significantly further from the mid-ocean ridge (Fig. 11b). Plume-ridge distances in the Pacific are

492   mostly >2000 km, which exceeds the maximum plume-ridge interaction distance of 1400 km

493   (Schilling, 1991). Most plumes in the Pacific exhibit the typical signatures of plume flow away from

494   the ridge, such as parabolic swell shapes (e.g., Society, Marquesas and Hawaii plumes; Ballmer et al.,

495   2013a; Ballmer et al., 2015; Cheng et al., 2015; Wolfe et al., 2009), and linear volcanic chains (Buff

496   et al., 2021; Clouard and Bonneville, 2005; Jackson et al., 2010). Age-progressive hotspots trails

497   indicate an absence of dominant ridge-ward flow. By contrast, most plumes in the Atlantic have been

498   close to the ridge since the opening of the ocean. These mantle plumes (e.g., Discovery, Iceland,

499   Tristan-Gough; O'Connor et al., 2012) did not move much since the breakup of the Atlantic. One

500   factor may be that the underlying plume generation zone (i.e., the edge of the African LLSVP) round

largely parallel to the Mid-Atlantic Ridge (Fig. 1) (Torsvik et al., 2006). In this case, plume-ridge

distance may play a critical role in the plume-ridge interaction, and could explain the striking

difference between the Pacific and Atlantic in terms of the proportion of plume-ridge interacting vs.

non-interacting systems. In addition, the rapid movement of the Pacific plate tends to inhibit

ridge-ward plume flow at a given plume-ridge distance. The distribution of interacting (stars) vs

non-interacting systems in Figure 11b is almost exactly as predicted by our models for the coupled

effects of plume-ridge distance and plate velocity. For example, we note that fast-spreading ridges

can still interact with adjacent plumes under the appropriate conditions. In the case of very short

plume-ridge distances, there is good evidence of plume-ridge interaction in the southern Pacific

ocean (e.g., Louisville plume; Conder et al., 2002; Toomey et al., 2002; Vlastélic and Dosso, 2005).

Based on a series of numerical modeling as well as geological and geophysical observations, we

conclude that mantle plumes in the Pacific are more likely to spread away from the ridge and into the

direction of plate motion than in the Atlantic and Indian Oceans. The tendency of fast plate velocities

to promote plume spreading away from the MOR through viscous drag may depend, however, on the

details of lithosphere-asthenosphere rheological coupling such as the presence of a weak decoupling

(e.g., melt) layer (Rychert et al., 2020). Further studies of plume spreading and plume-ridge

interaction are needed to shed light on the coupling of the plate-mantle system.
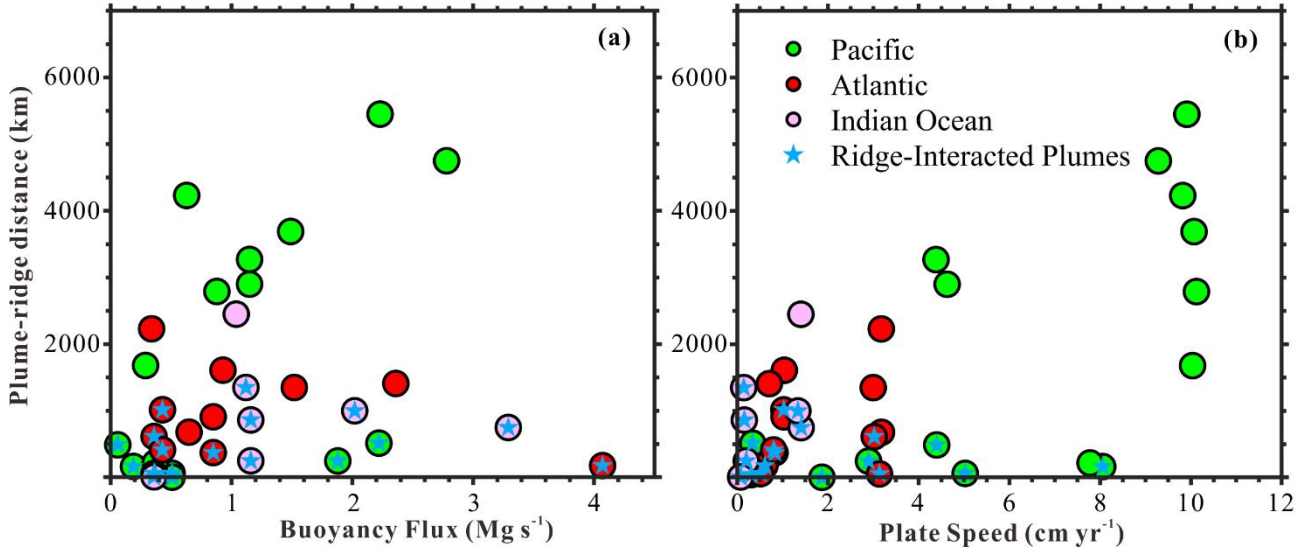
Figure 11. Buoyancy flux, plate speed and plume-ridge distance of mantle plumes in different

oceans. Mantle plumes in the Pacific, Atlantic and Indian Ocean are shown in green, red and pink

circles, respectively. Blue stars mark the ridge-interacted plumes according to Ito et al. (2003). **(a)**

Plot of plume-ridge distance and plume buoyancy flux. Data are from Hoggard et al. (2020). **(b)** Plot

of plume-ridge distance and plate speed at the location of plumes. Plume-ridge distance comes from

GPlates (Müller et al., 2016; Whittaker et al., 2015), and plate speed data comes from Becker et al.

(2015)

5   Conclusion

In this study, we explore the evolution of plume-ridge interaction with 2D thermomechanical

numerical models. Based on model results, we find that:

(1) Plume-ridge interaction is mainly governed by the competition between the effects of plume

spreading (overpressure in the plume-head stage), upward gravitationally-driven flow of the

plume along the base of the sloping lithosphere and plate shearing. These driving forces are

controlled by plume size, plume-ridge distance and the spreading rate of the mid-ocean ridge.

534 (2) MOR spreading does not only draw upwelling plumes into the spreading center, but also tends to

535 drag mantle plumes away from the ridge. Plume flow away from the ridge is favored by small

536 and/or distant plumes as well as fast spreading rates, whereas plume flow towards the ridge is

537 promoted by large and/or nearby plumes, as well as slow spreading rates.

538 (3) Considering the high plate velocity and typically large plume-ridge distances, mantle plumes in

539 the Pacific are more likely to be dragged away from the EPR than being drawn towards the ridge

540 center.

541

542

Code availability

The source numerical modeling code in this study is available from the corresponding author upon reasonable request.

Data availability

The data that support the findings of this study are available from the corresponding author upon reasonable request.

Author contribution

Fengping Pang performed all numerical models, interpreted results and wrote the manuscript. Jie Liao proposed the study, modify the code and contributed to rewriting and scientific discussion. Maxim D. Ballmer contributed with significant help in rewriting and scientific discussion. Lun Li participated in discussion and interpretations. All authors have read and edited draft versions of the paper and have approved the final version.

Competing interest

The authors declare that they have no conflict of interest.

Acknowledgement

This research is financially supported by NSFC projects (U1901214, 41974104, 91855208) and Guangdong project 2017ZT07Z066. We are grateful to Prof. Taras Gerya for his long-lasting guidance on our geodynamical modeling. We gratefully acknowledge Hongjian Fang for insightful

565   discussions. Numerical simulations were performed on the clusters of National Supercomputer

566   Center in Guangzhou (Tianhe-II).

567

568 **Reference**

569 Ballmer, M. D., Ito, G., Wolfe, C. J. and Solomon, S. C.: Double layering of a thermochemical

570 plume in the upper mantle beneath Hawaii, Earth Planet. Sci. Lett., 376, 155–164,

571 doi:10.1016/j.epsl.2013.06.022, 2013a.

572 Ballmer, M. D., Conrad, C. P., Smith, E. I. and Harmon, N.: Non-hotspot volcano chains produced

573 by migration of shear-driven upwelling toward the East Pacific Rise, Geology, 41(4), 479–482,

574 doi:10.1130/G33804.1, 2013b.

575 Ballmer, M. D., Ito, G. and Cheng, C.: Asymmetric dynamical behavior of thermochemical plumes

576 and implications for hawaiian lava composition, Geophys. Monogr. Ser., 208, 35–57,

577 doi:10.1002/9781118872079.ch3, 2015.

578 Barruol, G., Sigloch, K., Scholz, J. R., Mazzullo, A., Stutzmann, E., Montagner, J. P., Kiselev, S.,

579 Fontaine, F. R., Michon, L., Deplus, C. and Dyment, J.: Large-scale flow of Indian Ocean

580 asthenosphere driven by Réunion plume, Nat. Geosci., 12(12), 1043–1049,

581 doi:10.1038/s41561-019-0479-3, 2019.

582 Becker, T. W., Schaeffer, A. J., Lebedev, S. and Conrad, C. P.: Toward a generalized plate motion

583 reference frame, Geophys. Res. Lett., 42(9), 3188–3196, doi:10.1002/2015GL063695, 2015.

584 Buff, L., Jackson, M. G., Konrad, K., Konter, J. G., Bizimis, M., Price, A., Rose-Koga, E. F.,

585 Blusztajn, J., Koppers, A. A. P. and Herrera, S.: "Missing Links" for the Long-lived Macdonald and

586 Arago Hotspots, South Pacific Ocean, Geology, 49(5), 541–544, doi:10.1130/G48276.1, 2021.

587 Burov, E. and Cloetingh, S.: Erosion and rift dynamics: New thermomechanical aspects of post-rift

588 evolution of extensional basins, Earth Planet. Sci. Lett., 150(1–2), 7–26,

589 doi:10.1016/s0012-821x(97)00069-1, 1997.

Byerlee, J.: Friction of rocks, Pure Appl. Geophys. PAGEOPH, 116(4–5), 615–626, doi:10.1007/BF00876528, 1978.

Cheng, C., Allen, R. M., Porritt, R. W. and Ballmer, M. D.: Seismic constraints on a double-layered asymmetric whole-mantle plume beneath Hawai'i, Hawaiian Volcanoes From Source to Surf., 19–34, doi:10.1002/9781118872079.ch2, 2015.

Clouard, V. and Bonneville, A.: Ages of seamounts, islands, and plateaus on the Pacific plate, Spec. Pap. Geol. Soc. Am., 388, 71–90, doi:10.1130/0-8137-2388-4.71, 2005.

Conder, J. A., Forsyth, D. W. and Parmentier, E. M.: Asthenospheric flow and asymmetry of the East Pacific Rise, MELT area, J. Geophys. Res. Solid Earth, 107(B12), ETG 8-1-ETG 8-13, doi:10.1029/2001jb000807, 2002.

Cushman, B., Sinton, J., Ito, G. and Dixon, J. E.: Glass compositions, plume-ridge interaction, and hydrous melting along the Galapagos spreading center, 90.5 °wto 98 ° W, Geochemistry, Geophys. Geosystems, 5(8), doi:10.1029/2004GC000709, 2004.

Dalton, C. A., Langmuir, C. H. and Gale, A.: Geophysical and geochemical evidence for deep temperature variations beneath mid-ocean ridges, Science (80-.)., 344(6179), 80–83, doi:10.1126/science.1249466, 2014.

Douglass, J., Schilling, J. G. and Fontignie, D.: Plume-ridge interactions of the Discovery and Shona mantle plumes with the southern Mid-Atlantic Ridge (40°-55° S), J. Geophys. Res. Solid Earth, 104(B2), 2941–2962, doi:10.1029/98jb02642, 1999.

François, T., Koptev, A., Cloetingh, S., Burov, E. and Gerya, T.: Plume-lithosphere interactions in rifted margin tectonic settings: Inferences from thermo-mechanical modelling, Tectonophysics, 746(October 2015), 138–154, doi:10.1016/j.tecto.2017.11.027, 2018.

French, S. W. and Romanowicz, B.: Broad plumes rooted at the base of the Earth's mantle beneath major hotspots, Nature, 525(7567), 95–99, doi:10.1038/nature14876, 2015.

Gale, A., Dalton, C. A., Langmuir, C. H., Su, Y. and Schilling, J. G.: The mean composition of ocean ridge basalts, Geochemistry, Geophys. Geosystems, 14(3), 489–518, doi:10.1029/2012GC004334, 2013.

Geissler, W. H., Wintersteller, P., Maia, M., Strack, A., Kammann, J., Eagles, G., Jegen, M., Schloemer, A. and Jokat, W.: Seafloor evidence for pre-shield volcanism above the Tristan da Cunha mantle plume, Nat. Commun., (2020), doi:10.1038/s41467-020-18361-4, 2020.

Gerya, T.: Origin and models of oceanic transform faults, Tectonophysics, 522–523, 34–54, doi:10.1016/j.tecto.2011.07.006, 2012.

Gerya, T. V.: Three-dimensional thermomechanical modeling of oceanic spreading initiation and evolution, Phys. Earth Planet. Inter., 214, 35–52, doi:10.1016/j.pepi.2012.10.007, 2013.

Gerya, T. V. and Yuen, D. A.: Characteristics-based marker-in-cell method with conservative finite-differences schemes for modeling geological flows with strongly variable transport properties, Phys. Earth Planet. Inter., 140(4), 293–318, doi:10.1016/j.pepi.2003.09.006, 2003.

Gerya, T. V. and Yuen, D. A.: Robust characteristics method for modelling multiphase visco-elasto-plastic thermo-mechanical problems, Phys. Earth Planet. Inter., 163(1–4), 83–105, doi:10.1016/j.pepi.2007.04.015, 2007.

Gerya, T. V., Stern, R. J., Baes, M., Sobolev, S. V. and Whattam, S. A.: Plate tectonics on the Earth triggered by plume-induced subduction initiation, Nature, 527(7577), 221–225, doi:10.1038/nature15752, 2015.

Gülcher, A. J. P., Gerya, T. V., Montési, L. G. J. and Munch, J.: Corona structures driven by

plume–lithosphere interactions and evidence for ongoing plume activity on Venus, Nat. Geosci.,

13(8), 547–554, doi:10.1038/s41561-020-0606-1, 2020.

Hardarson, B. S., Fitton, J. G., Ellam, R. M. and Pringle, M. S.: Rift relocation - A geochemical and

geochronological investigation of a palaeo-rift in northwest Iceland, Earth Planet. Sci. Lett.,

153(3–4), 181–196, doi:10.1016/s0012-821x(97)00145-3, 1997.

Harmon, N., Forsyth, D. W., Weeraratne, D. S., Yang, Y. and Webb, S. C.: Mantle heterogeneity and

off axis volcanism on young Pacific lithosphere, Earth Planet. Sci. Lett., 311(3–4), 306–315,

doi:10.1016/j.epsl.2011.09.038, 2011.

Hoggard, M. J., Parnell-turner, R. and White, N.: Hotspots and mantle plumes revisited: Towards

reconciling the mantle heat transfer discrepancy, Earth Planet. Sci. Lett., 542, 116317,

doi:10.1016/j.epsl.2020.116317, 2020.

Ito, G., Lin, J. and Gable, C. W.: Interaction of mantle plumes and migrating mid-ocean ridges:

Implications for the Galfipagos plume-ridge system, , v, 1–3, 1997.

Ito, G., Lin, J. and Graham, D.: Observational and theoretical studies of the dynamics of mantle

plume-mid-ocean ridge interaction, Rev. Geophys., 41(4), doi:10.1029/2002RG000117, 2003.

Jackson, M. G., Hart, S. R., Konter, J. G., Koppers, A. A. P., Staudigel, H., Kurz, M. D., Blusztajn, J.

and Sinton, J. M.: Samoan hot spot track on a "hot spot highway": Implications for mantle plumes

and a deep Samoan mantle source, Geochemistry, Geophys. Geosystems, 11(12),

doi:10.1029/2010GC003232, 2010.

Jackson, M. G., Becker, T. W. and Steinberger, B.: Spatial Characteristics of Recycled and

Primordial Reservoirs in the Deep Mantle, Geochemistry, Geophys. Geosystems, 22(3),

doi:10.1029/2020GC009525, 2021.

656 Jellinek, A. M., Gonnermann, H. M. and Richards, M. A.: Plume capture by divergent plate motions:

657 Implications for the distribution of hotspots, geochemistry of mid-ocean ridge basalts, and estimates

658 of the heat flux at the core-mantle boundary, Earth Planet. Sci. Lett., 205(3–4), 361–378,

659 doi:10.1016/S0012-821X(02)01070-1, 2003.

660 Jiang, Q., Jourdan, F., Olierook, H. K. H., Merle, R. E. and Whittaker, J. M.: Longest continuously

661 erupting large igneous province driven by plume-ridge interaction, Geology, 1–3,

662 doi:10.1130/G47850.1, 2020.

663 Kincaid, C., Ito, G. and Gable, C.: Laboratory investigation of the interaction of off-axis mantle

664 plumes and spreading centres, Nature, 376(6543), 758–761, doi:10.1038/376758a0, 1995.

665 Kincaid, C., Schilling, J.-G. and Gable, C.: The dynamics of off-axis plume-ridge interaction in the

666 uppermost mantle, Earth Planet. Sci. Lett., 137(1–4), 29–43, doi:10.1016/0012-821X(95)00201-M,

667 1996.

668 Koppers, A. A. P., Becker, T. W., Jackson, M. G., Konrad, K., Müller, R. D., Romanowicz, B.,

669 Steinberger, B. and Whittaker, J. M.: Mantle plumes and their role in Earth processes, Nat. Rev.

670 Earth Environ., 2(6), 382–401, doi:10.1038/s43017-021-00168-6, 2021.

671 Lénat, J. F., Merle, O. and Lespagnol, L.: La réunion: An example of channeled hot spot plume, J.

672 Volcanol. Geotherm. Res., 184(1–2), 1–13, doi:10.1016/j.jvolgeores.2008.12.001, 2009.

673 Maia, M., Pessanha, I., Courrges, E., Patriat, M., Gente, P., Hémond, C., Janin, M., Johnson, K.,

674 Roest, W., Royer, J. Y. and Vatteville, J.: Building of the Amsterdam-Saint Paul plateau: A 10 Myr

675 history of a ridge-hot spot interaction and variations in the strength of the hot spot source, J. Geophys.

676 Res. Solid Earth, 116(9), 1–19, doi:10.1029/2010JB007768, 2011.

677 Mittelstaedt, E., Ito, G. and Behn, M. D.: Mid-ocean ridge jumps associated with hotspot magmatism,

Earth Planet. Sci. Lett., 266(3–4), 256–270, doi:10.1016/j.epsl.2007.10.055, 2008.

Mittelstaedt, E., Ito, G. and Van Hunen, J.: Repeat ridge jumps associated with plume-ridge

interaction, melt transport, and ridge migration, J. Geophys. Res. Solid Earth, 116(1), 1–20,

doi:10.1029/2010JB007504, 2011.

Mittelstaedt, E., Soule, S., Harpp, K., Fornari, D., McKee, C., Tivey, M., Geist, D., Kurz, M. D.,

Sinton, C. and Mello, C.: Multiple expressions of plume-ridge interaction in the Galápagos: Volcanic

lineaments and ridge jumps, Geochemistry, Geophys. Geosystems, 13(5),

doi:10.1029/2012GC004093, 2012.

Montelli, R., Nolet, G., Dahlen, F. A., Masters, G., Engdahl, E. R. and Hung, S. H.: Supporting

OnlineMaterial Timing, Science, 303(5656), 338–343, doi:10.1126/science.1092485, 2004.

Morgan, W. J.: Rodriguez, Darwin, Amsterdam, ..., A second type of Hotspot Island, J. Geophys.

Res. Solid Earth, 83(8), 5355–5360, 1978.

Müller, R. D., Roest, W. R. and Royer, J.-Y.: Asymmetric sea-floor spreading caused by

ridge–plume interactions, Nature, 396(6710), 455–459, doi:10.1038/24850, 1998.

Müller, R. D., Seton, M., Zahirovic, S., Williams, S. E., Matthews, K. J., Wright, N. M., Shephard, G.

E., Maloney, K. T., Barnett-Moore, N., Hosseinpour, M., Bower, D. J. and Cannon, J.: Ocean Basin

Evolution and Global-Scale Plate Reorganization Events since Pangea Breakup, Annu. Rev. Earth

Planet. Sci., 44, 107–138, doi:10.1146/annurev-earth-060115-012211, 2016.

Niu, Y.: Ridge suction drives plume-ridge interactions, , (October), doi:10.13140/2.1.4728.0961,

2014.

O'Connor, J. M., Jokat, W., Le Roex, A. P., Class, C., Wijbrans, J. R., Keßling, S., Kuiper, K. F. and

Nebel, O.: Hotspot trails in the South Atlantic controlled by plume and plate tectonic processes, Nat.

Geosci., 5(10), 735–738, doi:10.1038/ngeo1583, 2012.

Ranalli: Rheology of the Earth, 1995.

Ribe, N. M.: The dynamics of plume-ridge interaction: 2. Off-ridge plumes, , 101, 1996.

Ribe, N. M. and Christensen, U. R.: Three-dimensional modeling of plume-lithosphere interaction, ,

99, 669–682, 1994.

Ribe, N. M. and Christensen, U. R.: The dynamical origin of Hawaiian volcanism, Earth Planet. Sci.

Lett., 171(4), 517–531, doi:10.1016/S0012-821X(99)00179-X, 1999.

Ribe, N. M., Christensen, U. R. and Theißing, J.: The dynamics of plume-ridge interaction, 1:

Ridge-centered plumes, Earth Planet. Sci. Lett., 134(1–2), 155–168,

doi:10.1016/0012-821X(95)00116-T, 1995.

Rowley, D. B. and Forte, A. M.: Kinematics of the East Pacific Rise Retrodicted From Pacific and

Farallon/Nazca Subduction-Related Torques: Support for Significant Deep Mantle Buoyancy

Controlling EPR Spreading, J. Geophys. Res. Solid Earth, 127(2), 1–24, doi:10.1029/2020JB021638,

2022.

Rowley, D. B., Forte, A. M., Rowan, C. J., Glišović, P., Moucha, R., Grand, S. P. and Simmons, N.

A.: Kinematics and dynamics of the east pacific rise linked to a stable, deep-mantle upwelling, Sci.

Adv., 2(12), 1–19, doi:10.1126/sciadv.1601107, 2016.

Rychert, C. A., Harmon, N., Constable, S. and Wang, S.: The Nature of the

Lithosphere-Asthenosphere Boundary, J. Geophys. Res. Solid Earth, 125(10), 1–39,

doi:10.1029/2018JB016463, 2020.

Schilling, J. G.: Fluxes and excess temperatures of mantle plumes inferred from their interaction with

migrating mid-ocean ridges, Nature, 352(6334), 397–403, doi:10.1038/352397a0, 1991.

722 Sleep, N. H.: Lateral flow and ponding of starting plume material, J. Geophys. Res. Solid Earth,

723 102(B5), 10001–10012, doi:10.1029/97jb00551, 1997.

724 Small, C.: Observations of ridge-hotspot interactions in the Southern Ocean, J. Geophys. Res.,

725 100(B9), doi:10.1029/95jb01377, 1995.

726 Straume, E. O., Gaina, C., Medvedev, S., Hochmuth, K., Gohl, K., Whittaker, J. M., Abdul Fattah, R.,

727 Doornenbal, J. C. and Hopper, J. R.: GlobSed: Updated Total Sediment Thickness in the World's

728 Oceans, Geochemistry, Geophys. Geosystems, 20(4), 1756–1772, doi:10.1029/2018GC008115,

729 2019.

730 Toomey, D. R., Wilcock, W. S. D., Conder, J. A., Forsyth, D. W., Blundy, J. D., Parmentier, E. M.

731 and Hammond, W. C.: Asymmetric mantle dynamics in the MELT region of the East Pacific Rise,

732 Earth Planet. Sci. Lett., 200(3–4), 287–295, doi:10.1016/S0012-821X(02)00655-6, 2002.

733 Torsvik, T. H., Smethurst, M. A., Burke, K. and Steinberger, B.: Large igneous provinces generated

734 from the margins of the large low-velocity provinces in the deep mantle, Geophys. J. Int., 167(3),

735 1447–1460, doi:10.1111/j.1365-246X.2006.03158.x, 2006.

736 Turcotte, D. and Schubert, G.: Geodynamics, Cambridge University Press., 2014.

737 Vlastélic, I. and Dosso, L.: Initiation of a plume-ridge interaction in the South Pacific recorded by

738 high-precision Pb isotopes along Hollister Ridge, Geochemistry, Geophys. Geosystems, 6(5), 1–13,

739 doi:10.1029/2004GC000902, 2005.

740 Whittaker, J. M., Afonso, J. C., Masterton, S., Müller, R. D., Wessel, P., Williams, S. E. and Seton,

741 M.: Long-term interaction between mid-ocean ridges and mantle plumes, Nat. Geosci., 8(6),

742 doi:10.1038/NGEO2437, 2015.

743 Wolfe, C. J., Solomon, S. C., Laske, G., Collins, J. A., Detrick, R. S., Orcutt, J. A., Bercovici, D. and

744   Hauri, E. H.: Mantle shear-wave velocity structure beneath the Hawaiian hot spot, Science (80-.).,

745   326(5958), 1388–1390, doi:10.1126/science.1180165, 2009.

746   Yang, A. Y., Zhao, T. P., Zhou, M. F. and Deng, X. G.: Isotopically enriched N-MORB: A new

747   geochemical signature of off-axis plume-ridge interaction—A case study at 50°28′E, Southwest

748   Indian Ridge, J. Geophys. Res. Solid Earth, 122(1), 191–213, doi:10.1002/2016JB013284, 2017.

749
750